Journal Pre-proof

Nanoscale Insights into Ostwald Ripening of Clathrate Hydrates: A Correlative Atomic Force Microscopy and Molecular Dynamics Study

Fengyi Mi , Zhengtao Tao , Dongyan Liu , Bin Fang ,
Othonas A. Moultos , Thijs J.H. Vlugt , Fulong Ning

PII: S2667-3258(26)00474-7
DOI: https://doi.org/10.1016/j.fmre.2026.06.010
Reference: FMRE 1322

To appear in: *Fundamental Research*

Received date: 29 December 2025
Revised date: 29 May 2026
Accepted date: 9 June 2026

Please cite this article as: Fengyi Mi , Zhengtao Tao , Dongyan Liu , Bin Fang , Othonas A. Moultos , Thijs J.H. Vlugt , Fulong Ning , Nanoscale Insights into Ostwald Ripening of Clathrate Hydrates: A Correlative Atomic Force Microscopy and Molecular Dynamics Study, *Fundamental Research* (2026), doi: https://doi.org/10.1016/j.fmre.2026.06.010

Nanoscale Insights into Ostwald Ripening of Clathrate Hydrates: A Correlative Atomic Force Microscopy and Molecular Dynamics Study

Fengyi Mi[2,#], Zhengtao Tao[1,#], Dongyan Liu[1], Bin Fang[3], Othonas A. Moultos[4], Thijs J.H. Vlugt[4], Fulong Ning[1,*]

[1]National Center for International Research on Deep Earth Drilling and Resource Development, Faculty of Engineering, China University of Geosciences, Wuhan, Hubei 430074, China

[2]Key Laboratory of Solid Waste Treatment and Resource Reuse, Ministry of Education, Southwest University of Science and Technology, Mianyang 621010, Sichuan, China

[3]School of Marine Technology and Equipment, Hainan University, Haikou 570228, China

[4]Engineering Thermodynamics, Process & Energy Department, Faculty of Mechanical Engineering, Delft University of Technology, Leeghwaterstraat 39, Delft, 2628CB, the Netherlands

[#]These authors contributed equally to this work

[*]Author to whom correspondence should be addressed. nflzx@cug.edu.cn

Abstract

Sustainable hydrate-based technologies generally involve hydrate coarsening and growth. The Ostwald ripening observed during hydrate coarsening has important implications for sustainable hydrate-based technologies, but the exact mechanism remains unclear. Herein, systematic molecular dynamics (MD) simulations and atomic force microscopy (AFM) experiments are combined to investigate the structural transformation of THF hydrate. Our nanoscale investigation not only confirmed this phenomenon but also revealed its unique driving mechanism: a key size-dependent transition in the decomposition behavior of small hydrate particles. The decomposition of small hydrate particles goes through two stages, namely the continuous decomposition stage and the collapse decomposition stage. In the continuous decomposition stage, small hydrate nanoparticles decompose from the outside to the inside in sequence. When the radius of the hydrate nanoparticles reaches about 1 nm, the hydrate nanoparticles transition from the continuous decomposition stage to the collapse decomposition stage. In the collapse decomposition stage, the outside and inside of the hydrate nanoparticle will decompose together. This nanoscale insight helps in understanding the formation mechanism of clathrate hydrate and advances the development of sustainable hydrate-based technologies, such as CO_2 sequestration and seawater desalination.

Keywords: Ostwald ripening; THF hydrate; Hydrate morphology; Hydrate growth; Atomic force microscope; Molecular dynamics simulation

Table of Contents (TOC)/Graphical Abstract

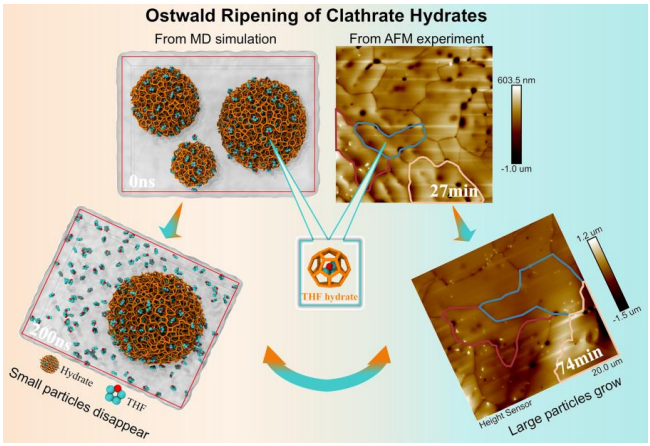

1. Introduction

Clathrate hydrates (also referred to as hydrates) are hydrogen bond-based structures in which small guest molecules (*e.g.*, H_2, CH_4, CO_2, C_3H_8, THF) are trapped in a hydrogen-bonded network formed by the oriented arrangement of water molecules [1-3]. Clathrate hydrates exhibit high storage capacity under the conditions of moderate temperature and high pressure[1]. For example, the 1 m^3 of CH_4 hydrate contains up to 160 m^3 of CH_4 gas, and the capacity of H_2 storage in clathrate hydrate reaches 5 wt% [4]. Clathrate hydrates containing different guest molecules also exhibit different phase equilibrium conditions. The unique properties and formation conditions of clathrate hydrates have evolved a series of sustainable hydrate-based technologies, such as CO_2 sequestration [5, 6], gas separation [7], H_2 storage and transportation [8, 9], natural gas solidification storage [10, 11], seawater desalination [12], juice concentration [13], and wastewater treatment [14]. These hydrate-based technologies all rely on clathrate hydrate formation. However, the slow formation rate of clathrate hydrates, low water-hydrate conversion rate, and limited mass transfer of guest molecules have hindered the industrialization of these sustainable hydrate-based technologies [15-18]. These limiting factors can be traced back to the formation mechanism of clathrate hydrate.

The formation and evolution of crystalline structures proceed through multiple pathways, including classical monomer-by-monomer growth from solution or melt, aggregation of pre-formed clusters, and oriented attachment of crystalline subunits. While these mechanisms can contribute to the initial stages of nucleation and growth, the late-stage evolution of clathrate hydrates is often characterized by grain coarsening. Among these processes, Ostwald ripening stands out as a critical size-dependent transformation driven by the Gibbs-Thomson effect [19, 20]. As the molecules on the surface of the crystal are less stable than those inside the crystal, the large crystals are energetically favored over the small ones, which manifests as the small crystals dissolving first and then redepositing onto the large crystals to minimize surface area and surface free energy.

Similar Ostwald ripening phenomena have been observed in previous literatures on the growth and coarsening of clathrate hydrate [21-27]. Experimental investigations by Dai and co-workers suggested that Ostwald ripening in mature hydrate-bearing coarse-grained sediments would promote patchy hydrate distribution [28]. The experimental investigation of Chen *et al.* by using X-ray diffraction showed that Ostwald ripening could change the pore habits of xenon and methane hydrates in hydrate-bearing sediments, resulting in xenon and methane hydrates heterogeneous distribution in hydrate-bearing sediments in pore and core scales [29, 30]. Visualization experiment results of Oya and co-workers observed that pointed ends of the CO_2 hydrate disappear and then recrystallize from 37 minutes to 112 minutes [31]. In the CT image with 40-μm resolution, Lei *et al.* found that small hydrate exists and could not merge into large hydrate when the intrapores are quite large, which meant that Ostwald ripening did not occur in a short time [32]. Core-scale laboratory experiments can only observe phenomena similar to Ostwald ripening, but cannot provide direct evidence. Experiments entering the nanoscale can help us understand the Ostwald ripening mechanism in the formation and coarsening process of gas hydrate from the molecular scale. Atomic force microscopy (AFM) stands out and can provide nanometer-level resolution [33-36]. Huang *et al.* observed through AFM images that the larger THF hydrate particles in the center grew slowly, while the small hydrate particles underwent dynamic formation-dissociation [37, 38]. Based on the AFM results, Li *et al.* speculated that the surface morphology formed by Ostwald ripening in polycrystalline THF hydrate influences the thickness of the quasi-liquid layer on the hydrate surface [39]. Molecular dynamics (MD) simulation is a widely utilized tool with low cost, high safety, and environmental friendliness compared to laboratory experiments [40-42]. Some MD simulations have been used to confirm the Ostwald ripening of gas cluster growth [43], ice crystallization [44], and nanobubbles coalescence [45]. Similar Ostwald ripening phenomena were observed in our prior MD simulations for CH_4 hydrate formation in marine sediments [46].

Currently, previous studies have speculated that Ostwald ripening is one of the important characteristics of gas hydrate formation, and there is no evidence that Ostwald ripening exists in the formation and coarsening process of gas hydrate. In this study, systematic MD simulations and AFM experiments are performed to investigate the structural transformation of clathrate hydrate in aqueous solution and at the air-water interface. We provide nanoscale evidence that Ostwald ripening occurs during the growth and coarsening of clathrate hydrate. Our results show that the decomposition of small hydrate particles goes through two stages, namely the continuous decomposition stage and the collapse decomposition stage. This nanoscale insight helps in understanding the formation mechanism of clathrate hydrate and advances the development of sustainable hydrate-based technologies (*i.e.*, H_2/CH_4 storage and transportation, CO_2 sequestration, seawater desalination, and wastewater treatment). The fundamental insights provided here regarding the behavior of metastable hydrate nanoparticles may support further understanding of sustainable hydrate-based technologies. This paper is organized as follows: Section 2 provides a short description of the MD simulation techniques and the AFM apparatus. Section 3

investigates the Ostwald ripening of clathrate hydrate. Concluding remarks are presented in Section 4.

2. Simulation Models and Methods

2.1 Atomic force microscopy apparatus and methods

Hydrate formation typically undergoes a period of nucleation, crystal growth, and grain coarsening, during which the Ostwald ripening phenomenon occurs. We employed in situ atomic force microscopy (AFM) to observe hydrate surface structures at the nanoscale, uncovering the dynamic evolution mechanisms of hydrate grains during Ostwald ripening. As shown in our prior studies [33], static topography imaging can resolve surface features such as grain size, intercrystalline gaps, and surface roughness, which are critical for understanding fundamental hydrate properties and the mechanisms of additives (e.g., anti-agglomerants, surfactants). However, hydrates undergo dynamic changes during nucleation, growth, and stabilization. Due to challenges in maintaining stringent growth conditions and surface quality, studies on these dynamic processes remain scarce. This underscores the necessity for meticulous sample preparation and advanced characterization techniques. The experimental observations were performed using a cryogenic atomic force microscopy (AFM) in situ observation system, modified from a Bruker Dimension Edge AFM, as shown in Figure 1(a). This system enables hydrate sample preparation and characterization under temperature-controlled conditions ranging from -190°C to room temperature. To quantify instrumental uncertainty, the noise levels were monitored and found to be less than 0.5 nm in the lateral plane and less than 0.2 nm in the vertical direction, ensuring the high-fidelity capture of nanoscale surface dynamics.

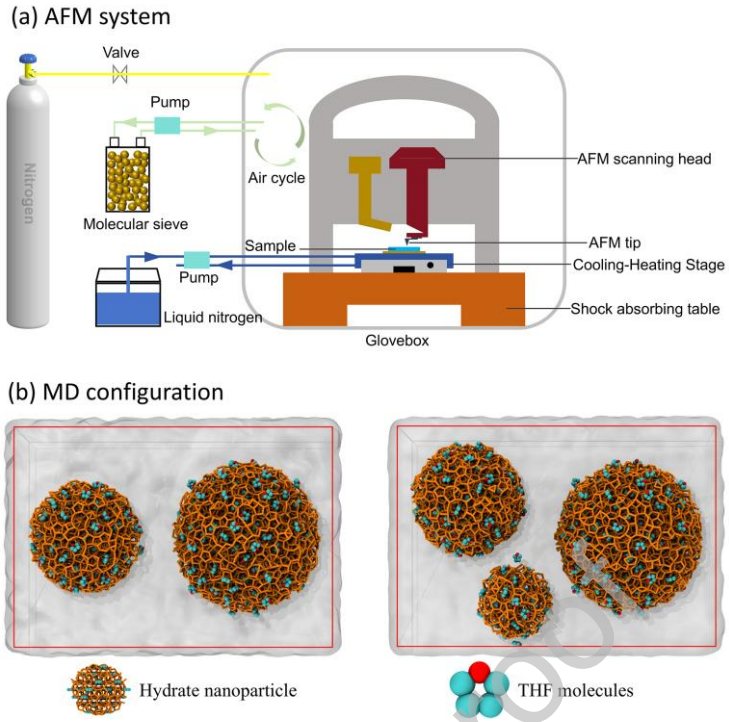

Figure 1. (a) Schematic diagram of the cryogenic atomic force microscopy system. (b) Initial configuration of MD simulations for the NP_{2THF} and NP_{3THF} systems.

Ultrapure water (resistivity: 18.25 MΩ·cm) was prepared using a purification system (Wuhan Pinguan Instrument Co., Ltd., China). Tetrahydrofuran (THF, 99.9% purity) was supplied by Meryer (Shanghai) Biochemical Technology Co., Ltd. Mica substrates were manufactured by TOHSO Trading Co., Ltd. Sample preparation and analytical workflow as follows: (1) A 22 vol% THF solution (5 mL) was prepared. Before experiments, the glove box was pre-dehumidified through 24-hour circulation to maintain a dew point below 208.15 K. (2) After stabilizing the sample stage temperature at 278.15 K, 25 μL of the 22% THF solution was deposited onto the mica substrate. The temperature was then reduced to 258.15 K at a rate of 10°C/min, during which hydrate spontaneously nucleated and grew. (3) Following a 5-minute stabilization period at 258.15 K, the sample was positioned under the AFM scanner. Surface topography of the hydrate was acquired in tapping mode, with continuous imaging of the same microregion without stage movement. (4) AFM topography images were flattened using NanoScope Analysis software and subsequently processed in ImageJ to quantify hydrate grain areas and population statistics.

2.2 Molecular dynamics simulation models and methods

THF hydrate is one of the clathrate hydrates with THF molecules as guests. THF has excellent formation conditions (*e.g.*, low formation pressure, mild formation temperature) compared to CH_4, CO_2 hydrates [39, 47]. To explore the Ostwald ripening that exists in the structural transformation of THF hydrates, three types of THF

hydrate nanoparticles were created with diameters of 6, 4.5, and 3 nm, respectively. Two different systems were created, containing two THF hydrate nanoparticles and three THF hydrate nanoparticles, respectively. The two systems were labeled as NP_{2THF} and NP_{3THF}, respectively. In the NP_{2THF} system, two THF hydrate nanoparticles with diameters of 6 nm and 4.5 nm were placed in a box of size 90 × 85 × 110 Å, which was filled with H_2O molecules. In the NP_{3THF} system, THF hydrate nanoparticles with diameters of 6 nm, 4.5 nm, and 3 nm were placed in a box of size 90 × 85 × 110 Å, which was filled with H_2O molecules. The NP_{2THF} system contains 26,349 H_2O molecules and 294 THF molecules, while the NP_{3THF} system contains 26,349 H_2O molecules and 327 THF molecules (see Figure 1(b) and Table 1). To reduce the randomness of the structural transformation of THF hydrate, the NP_{2THF} and NP_{3THF} systems were repeated five times.

Table 1. Number of molecules of each species for the two different simulations.

	T = 258.15 K and P = 1 bar			
System	N_{THF}	N_{H_2O}	Time	Repeated
NP_{2THF}	294	26349	100 ns	5
NP_{3THF}	327	26349	200 ns	5

OPLS-AA [48] and TIP4P-Ice [49] force fields were used for THF and H_2O molecules, respectively. All force field details were listed in Table S1 in the Supporting Information. The leap-frog integrator algorithm with a time step of 2.0 fs was used, and the trajectories were saved every 10 ps. The particle mesh Ewald (PME) method with a cutoff range of 10 Å was used to determine the long-range Coulombic interactions using a grid spacing of 1.2 Å. The Lorentz-Berthelot mixing rules were used for the cross interactions. The cutoff range of 10 Å was applied to compute the Van der Waals forces. Periodic boundary conditions were assigned in all directions. The isothermal-isobaric *NPT* ensemble balance for NP_{2THF} (100 ns) and NP_{3THF} (200 ns) systems was carried out at a constant temperature (T = 258.15 K) using Nosé-Hoover [50] temperature coupling, and at a constant pressure (P = 1 bar) using Parinello-Rahman [51] pressure coupling. This temperature and pressure condition is consistent with the AFM experiment in this study. All the simulations above were performed using the GROMACS 2022 [52] package.

3. Results and Discussions

3.1 Ostwald ripening of clathrate hydrate from AFM experiments

Unlike conventional static observations, this study conducted continuous in situ monitoring of the same microregion on THF hydrate surfaces to probe dynamic microstructural evolution. As shown in Figure 2(a-e), the AFM 2D height images (50 μm × 50 μm) show a polycrystalline THF hydrate sample prepared at 258.15 K, composed of irregularly shaped monocrystalline grains (*e.g.*, pentagons, hexagons, or irregular polygons) with

distinct grain boundaries (Figure 2(a)). As the hydrate samples are placed for long periods, significant structural changes are observed, especially in grain size, population, and morphology. Specifically, the highlighted grains A, B, and C exhibit substantial growth and coalescence, whereas smaller adjacent grains indicated by white arrows progressively diminish in area and ultimately vanish, providing visual confirmation of Ostwald ripening (Figure 2(a-e)).

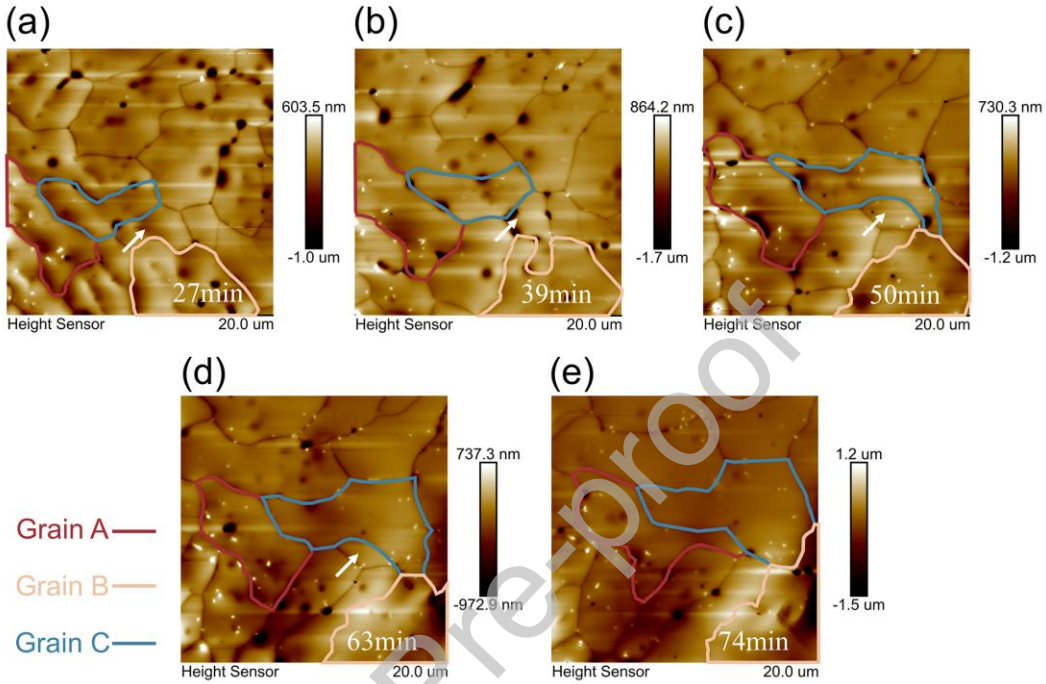

Figure 2. (a-e) Time evolution of surface height images of THF hydrate surfaces at different times, *i.e.*, 27 min, 39 min, 50 min, 63 min, and 74 min. The red, yellow, and blue lines represent the crystal sizes of grains A, B, and C, respectively. The white arrows represent the crystal diminishing in area and ultimately vanish.

To quantify microstructural evolution, grain characteristics are statistically analyzed using ImageJ (Figure 3(a-b)). The quantitative results reveal that the average size of individual hydrate grains increases as the total population decreases. We track and count each grain in the image in order from the largest to the smallest grain area. We observe that during the period of 74 minutes, the grain count decreases from 27 (at 27 min) to 20, indicating that 7 hydrate grains are disappearing. Moreover, the largest grain area expands from 1193.9 to 1520.4 μm^2 (Figure 3(a)), which suggests that the largest hydrate grain gradually grows and coarsens. After stabilizing at 258.15 K for 5 minutes (confirmed by Raman spectroscopy), Morphologically, the hydrate grains predominantly maintain stable irregular polygonal shapes, such as pentagons and hexagons, which are characteristic of mature polycrystalline films undergoing coarsening. THF hydrate formation is complete, yet grain rearrangement persists, *i.e.*, these large hydrates continue growing and coarsening, whereas small ones diminish in size. This dynamic process reveals the instability of grain boundaries, which drives the recrystallization of THF hydrate. Notably, grains A, B, and C exhibit distinct growth trends (Figure 3(b)). Grain C grows continuously all the time, while grains A and B

initially expand rapidly and then slowly (Figure 3(b)). This difference may be attributed to the differences in the grain boundaries of the hydrate (Figure 2(a-e)). The irregular morphology of these grains suggests that the coarsening of large hydrate follows a continuous growth mode rather than a faceted layered or spiral mechanism. This behavior is driven by the dynamic exchange of molecules at the interface to achieve a more stable, low-energy configuration.

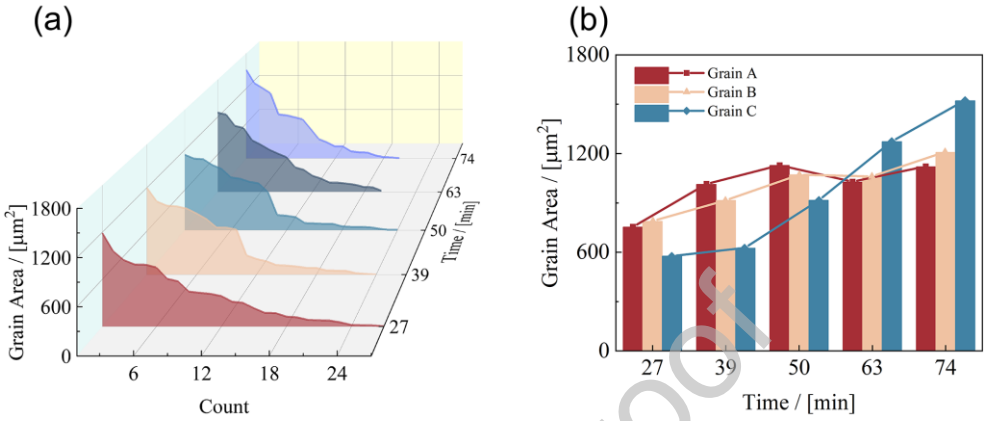

Figure 3. (a) The evolution of the total area and number of THF hydrate grains. The multi-colored curves represent different test times. (b) The evolution of grain areas for three different THF hydrate grains, *i.e.*, grains A, B, and C, is shown in Figure 2.

Current theories propose the existence of a dynamic quasi-liquid layer (QLL) at hydrate-gas interfaces, which exhibits fluid-like behavior[39, 53, 54]. Temperature gradients between the sample and environment, combined with THF volatility, may drive gradual QLL evaporation. To maintain stability, THF hydrate near the QLL partially dissociates to replenish the QLL, while recrystallization occurs at the QLL-hydrate interface, facilitating grain coarsening via Ostwald ripening. This implies that the interfacial instabilities induced by temperature and mass transfer gradients trigger a dynamic balance of dissociation and recrystallization, where Ostwald ripening controls grain coarsening to stabilize the system. Similar behavior was observed in ice under analogous experimental conditions (see Figures S1-S2), suggesting a universal mechanism for crystalline stability at interfaces. Figure 4 illustrates the dynamic morphological evolution of ice crystals at the air-solid interface over a period of 91 minutes, serving as a comparative reference to the THF hydrate system. The time-resolved AFM height images reveal a distinct polycrystalline structure characterized by irregular grains and sharp boundaries. As the observation progresses from 47 to 91 minutes, a clear coarsening phenomenon is evident: larger ice grains expand significantly while adjacent smaller grains gradually shrink or merge. This structural rearrangement, driven by the minimization of interfacial free energy, mirrors the behavior observed in THF hydrates, thereby confirming that Ostwald ripening is a universal mechanism governing the stability and growth of crystalline water-based systems under interfacial instability. These findings provide critical insights into hydrate interfacial dynamics and strategies for enhancing hydrate system stability.

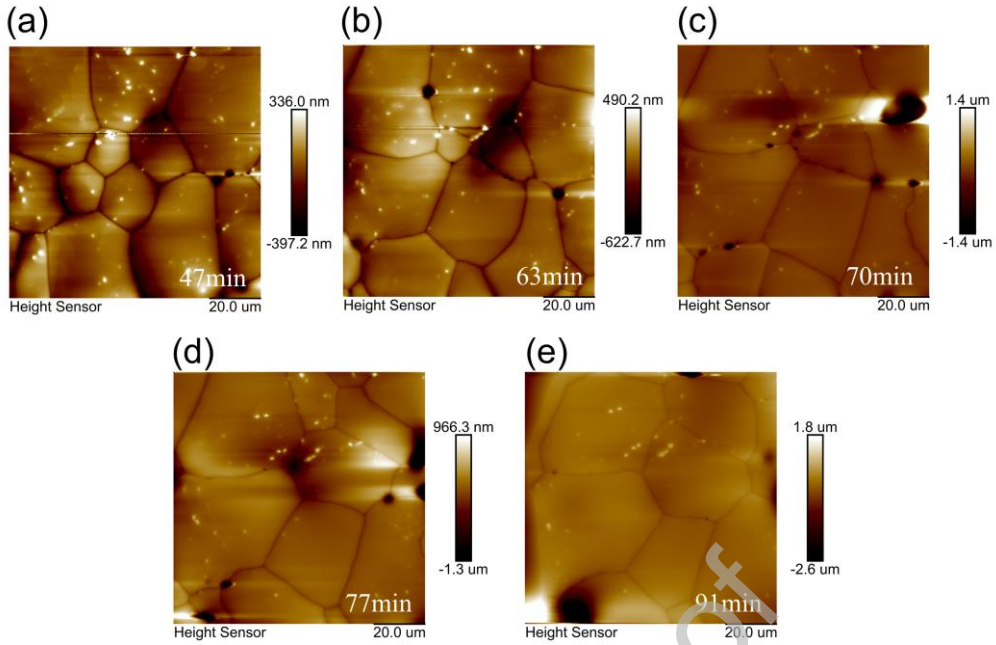

Figure 4. Time evolution of surface height images of ice surfaces at different times, *i.e.*, 47 min, 63 min, 70 min, 77 min, and 91 min.

3.2 Ostwald ripening of clathrate hydrate from MD simulations

The experimental observations presented in Section 3.1 provide definitive evidence of Ostwald ripening through the evolution of hydrate grain boundaries and population statistics at the micrometer scale. However, the specific molecular pathways and the energetic drivers of these structural transformations require higher temporal and spatial resolution than what experimental topography can currently provide. Consequently, molecular dynamics simulations are employed to bridge this gap by resolving the atomic-scale kinetics of THF hydrate nanoparticles. This multiscale approach allows for the correlation of long-term grain coarsening observed via AFM with the rapid, size-dependent decomposition mechanisms occurring at the individual cage level, thereby providing a comprehensive understanding of the ripening process.

From the MD simulation results, it is observed that THF hydrate nanoparticles in aqueous solution also undergo an Ostwald ripening phenomenon. These spherical nanoparticles are employed to represent the individual monocrystalline grains that constitute the polycrystalline hydrate film characterized in the AFM experiments. By utilizing a spherical geometry, the simulations can isolate the size-dependent stability of the hydrate lattice from complex grain boundary interactions, thereby providing a fundamental molecular basis for the coarsening behavior observed at the micrometer scale. The coarsening process of THF hydrates for the NP_{2THF} systems is shown in Figure 5(a-f). As THF hydrate coarsens, $D_{4.5}$ THF hydrate nanoparticles gradually become small and even disappear, whereas D_6 THF hydrate nanoparticles remain at a large size and do not disappear (Figure 5(a-f)). During the 100 ns of THF hydrate coarsening, no new THF hydrate nanoparticles appeared, and the $D_{4.5}$ THF

hydrate nanoparticles did not disintegrate into multiple small THF hydrate nanoparticles (Figure 5(a-f)). To further reveal the dynamic evolution of the two THF hydrate nanoparticles, the local tetrahedral order parameter of water molecules (F_4) from the center of the nanoparticles, the volume/surface area, and the number of intact hydrate cages are computed in Figure 6(a-d) and Figures S3-S7 in the supporting information. Because the structural integrity of these nanoparticles relies on the clathrate framework enclosing the guest molecules, tracking the total number of fully formed hydrate cages provides a direct, quantitative measure of the THF hydrate nanoparticle size and thermodynamic stability. The value of F_4 far from the center of the $D_{4.5}$ THF hydrate nanoparticle is lower than that close to the center (Figures 6(a) and S3(a-e)). This disordered shell effectively represents the microscopic equivalent of the Quasi Liquid Layer identified through AFM. The enhanced mobility of water and guest molecules within this interfacial region facilitates the preferential decomposition of smaller nanoparticles and the subsequent diffusion of tetrahydrofuran molecules into the aqueous phase. The value of F_4 decreases from the outside to the inside of the sphere $D_{4.5}$ THF hydrate nanoparticle as a function of time (Figures 6(a) and S3(a-e)). This indicates that the small spherical THF hydrate nanoparticles decompose from the outside to the inside in sequence. Since the outer surfaces of THF hydrate nanoparticles are in direct contact with the aqueous solution and are more unstable than the inside, the surface of the THF hydrate nanoparticles decomposes preferentially. Moreover, there is a difference in THF concentration between the hydrate and the aqueous solution, so the THF molecules in the THF hydrate nanoparticle diffuse into the aqueous phase to increase the THF mole fraction in the aqueous phase (see Figure S8(a-e)).

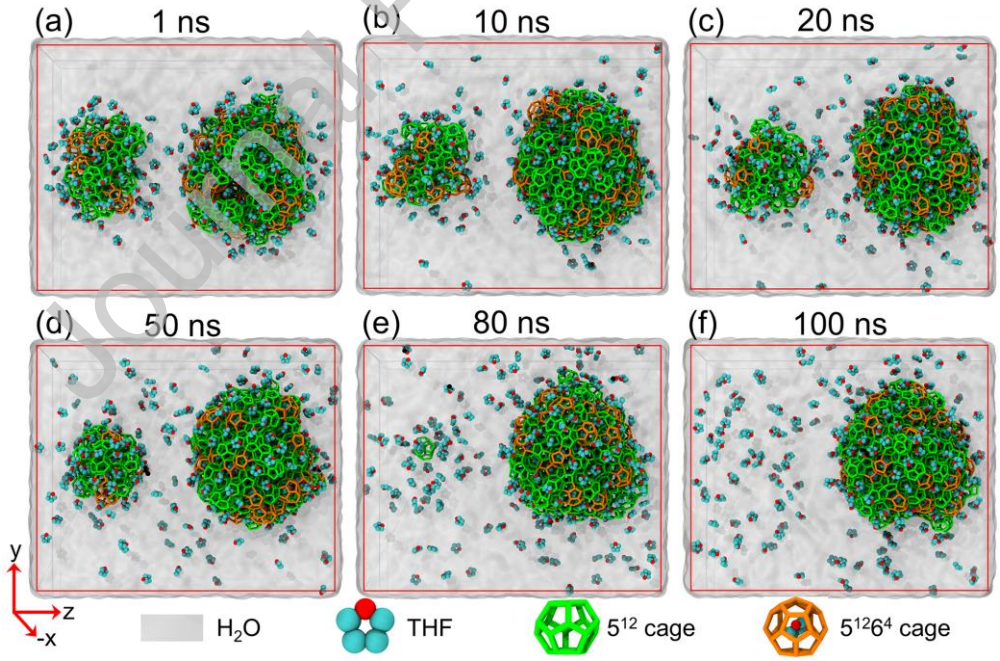

Figure 5. (a-f) Simulation snapshots showing the coarsening process of THF hydrates for the NP_{2THF} systems at different simulation times, *i.e.*, 1 ns, 10 ns, 20 ns, 50 ns, 80 ns, and 100 ns. THF is displayed as cyan (C atom) and red (O atom). Bonds of different colours represent seven types of hydrate cages, *i.e.*, green for 5^{12}, and orange for $5^{12}6^4$.

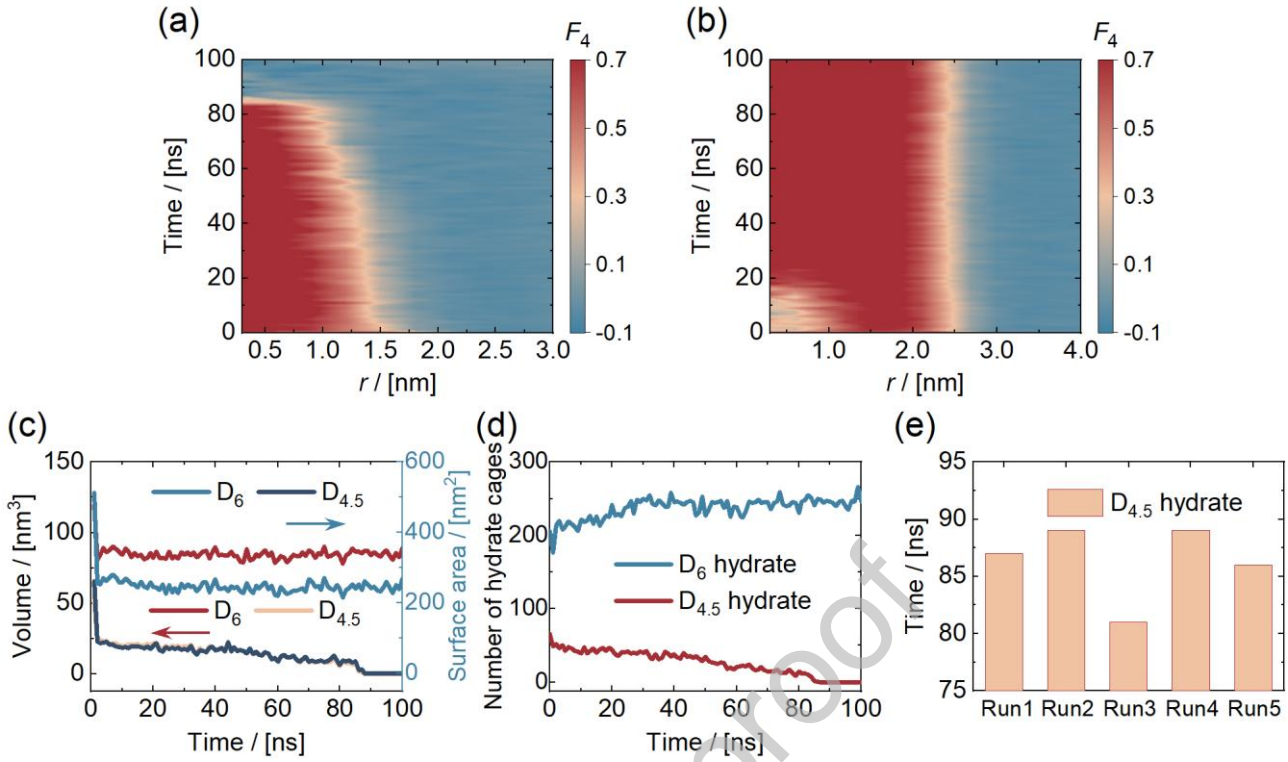

Figure 6. Time evolution of the F_4 from the center of the (a) $D_{4.5}$ and (b) D_6 THF hydrate nanoparticle for the NP_{2THF} system. The r = 0 nm represents the center of the THF hydrate nanoparticle, while sampling was averaged for 1 ns. Time evolution of the (c) volume/surface area of the THF hydrate nanoparticles and (d) the number of cages in the two nanoparticles for the NP_{2THF} system. (e) The time required for the complete disappearance of the $D_{4.5}$ THF hydrate nanoparticles in the five repeated simulations.

The volume of the $D_{4.5}$ THF hydrate nanoparticles gradually decreases to zero (Figure 5(a-f) and 6(c)), which means that the small THF hydrate nanoparticles will gradually become smaller and eventually disappear. The same insights can be obtained from the F_4, surface area, number of hydrate cages, and number of water molecules in the cages of the $D_{4.5}$ THF hydrate nanoparticles (Figures 6(a-d), S3(a-e), S6(a-e), S7(a-e), and S9(a-e)). It is worth noting that the decomposition of small hydrate particles goes through two stages, namely the continuous decomposition stage and the collapse decomposition stage. The continuous decomposition stage is mainly during the period of 0 - 80 ns. The $D_{4.5}$ THF hydrate nanoparticles continuously decompose from the outside to the inside, and the decomposition rate is relatively stable (Figure 6(a, c, and d)). The collapse decomposition stage mainly occurs during the period of 80 - 100 ns (Figure 6(a, c, and d)). When the decomposition continues from the outside to the inside to a radius of about 1 nm (Figures 6(a) and S3(a-e)), the outside and inside of the $D_{4.5}$ THF hydrate nanoparticle will decompose together, *i.e.*, collapse decomposition. At this critical size (1 nm), the cooperative hydrogen bond network that maintains the clathrate cages becomes globally distorted due to the high surface to volume ratio. Simulation data demonstrate that the F_4 order parameter, which characterizes the tetrahedrality of water molecules, drops simultaneously across the entire nanoparticle volume during this stage.

This synchronized destabilization of the water framework results in the abrupt disintegration of the protective cages, allowing for the rapid and simultaneous diffusion of guest molecules from both the core and the surface into the surrounding solution. This transition signifies a shift from a surface-controlled process to a volume-controlled lattice collapse.

During the decomposition of $D_{4.5}$ THF hydrate nanoparticles, D_6 THF hydrate nanoparticles undergo structural reorganization and growth (Figure 5(a-f)). The spherical THF nanoparticles are obtained by cutting standard SII hydrate, so the outer surface of the spherical THF hydrate is metastable. During the 0 - 1 ns of THF hydrate coarsening, the outer surface of the D_6 THF hydrate nanoparticle will quickly reorganize to a more stable state. The surface area of the D_6 THF hydrate nanoparticle will quickly decrease to a stable value (Figures 6(c) and S6(a-e)), which is an optimization process. This initial contraction is necessary to stabilize the metastable surface created during the generation of the spherical model from bulk crystals. Once this optimization is complete, the D_6 nanoparticle can dissolve smaller particles. As the $D_{4.5}$ THF hydrate nanoparticles decompose, the number of hydrate cages in the D_6 THF hydrate nanoparticles increases slightly, indicating that the large THF hydrate nanoparticles begin to grow and coarsen after the initial reorganization (Figures 6(d) and S7(a-e)). This synchronized evolution of particle sizes confirms that the system is undergoing Ostwald ripening rather than simple independent dissociation. This phenomenon can also be confirmed by the F_4, number of hydrate cages, volume/surface area, and number of water molecules in the cages of the D_6 THF hydrate nanoparticles (Figures 6(a-c), S4-S7, and S9(a-e)). These results show that the decomposition of small THF hydrate nanoparticles is beneficial to the coarsening and growth of large THF hydrate nanoparticles. To verify the repeatability of the simulation results, the NP_{2THF} system was repeated five times. This optimization involves the local rearrangement of water and guest molecules within the existing boundaries of the nanoparticle. Specifically, the number of hydrate cages increases because previously disordered regions or vacant cavities within the D_6 cluster gradually transform into complete clathrate cages through structural reorganization (Figure 6(d)). Consequently, the total cage count can rise even as the overall volume and surface area remain relatively constant or experience slight initial contraction (Figures 6(c-d)). The time required for the complete disappearance of the $D_{4.5}$ THF hydrate nanoparticles is shown in Figure 6(e). It shows that the $D_{4.5}$ THF hydrate nanoparticles disappear during the 80 - 90 ns of THF hydrate coarsening (Figure 6(e)). The statistical reliability of the ripening process is confirmed by the results of five independent simulation runs. For the NP_{2THF} system, the complete disappearance of the $D_{4.5}$ THF hydrate nanoparticles was observed at a mean time of 86.4 ± 2.3 ns (Figure 6(e)). The low standard deviation indicates that the decomposition kinetics in the two-particle system are highly reproducible and primarily driven by the localized thermodynamic instability of the smaller particle relative to its larger counterpart. Ostwald ripening occurs in the coarsening and growth of THF hydrate for other repeated simulations (Figure S10(a-l)). During the 0 - 100 ns of THF hydrate coarsening, THF hydrate nanoparticles are mainly 5^{12} and $5^{12}6^4$ cages

(Figure S11-S12), which is consistent with the characteristics of SII-type hydrate. The evidence from our simulations clearly distinguishes Ostwald ripening from other growth mechanisms like aggregation or oriented attachment. Throughout the coarsening process, we observe that smaller nanoparticles diminished in size and disappeared without merging as stable units into the larger particles. The growth of larger hydrate is sustained by the mass transfer of guest and water molecules released from the dissolving smaller particles, which is the defining characteristic of the Ostwald ripening pathway.

In the system with three THF hydrate nanoparticles (NP_{3THF}), Ostwald ripening also appears in the coarsening and growth of THF hydrates. The coarsening process of the NP_{3THF} system is shown in Figure 7(a-f). In the NP_{3THF} system, both D_3 and $D_{4.5}$ THF hydrate nanoparticles gradually decompose and eventually disappear, while D_6 THF hydrate nanoparticles still exist (Figures 7(a-f) and S13(a-l)). D_3 THF hydrate nanoparticles decompose faster than $D_{4.5}$ THF hydrate nanoparticles, which once again confirms that small-sized THF hydrate nanoparticles are more unstable than large-sized THF hydrate nanoparticles (Figures 7(a-f) and S13(a-l)). For the smallest nanoparticles, D_3 THF hydrate nanoparticles decompose quickly and are dissolved in water (Figure 7(a-b)). The radius of D_3 THF hydrate nanoparticles is so small that they collapse and decompose directly in the solution. The volume/surface area, the number of hydrate cages, and the number of water molecules in the cages of D_3 THF hydrate nanoparticles all decrease to zero in a short time (Figures 8(c-d) and S14-S17). The decomposition of $D_{4.5}$ THF hydrate nanoparticles also goes through two decomposition stages, *i.e.*, the continuous decomposition stage and the collapse decomposition stage. During the 0 - 55 ns of THF hydrate coarsening, $D_{4.5}$ THF hydrate nanoparticles continuously decompose from the outside to the inside (Figures 8(a) and S18(a-e)). At 55 ns, the radius of the $D_{4.5}$ THF hydrate nanoparticles is only about 1 nm, and the $D_{4.5}$ THF hydrate nanoparticles transition from the continuous decomposition stage to the collapse decomposition stage (Figures 8(a) and S18(a-e)). During the 55 - 65 ns of THF hydrate coarsening, the F_4, volume/surface area, number of hydrate cages, and number of water molecules in the cages of the $D_{4.5}$ THF hydrate nanoparticles all decrease rapidly to 0 (Figures 8(a-d) and S14-S18), indicating that the $D_{4.5}$ THF hydrate nanoparticles completely decompose and disappear.

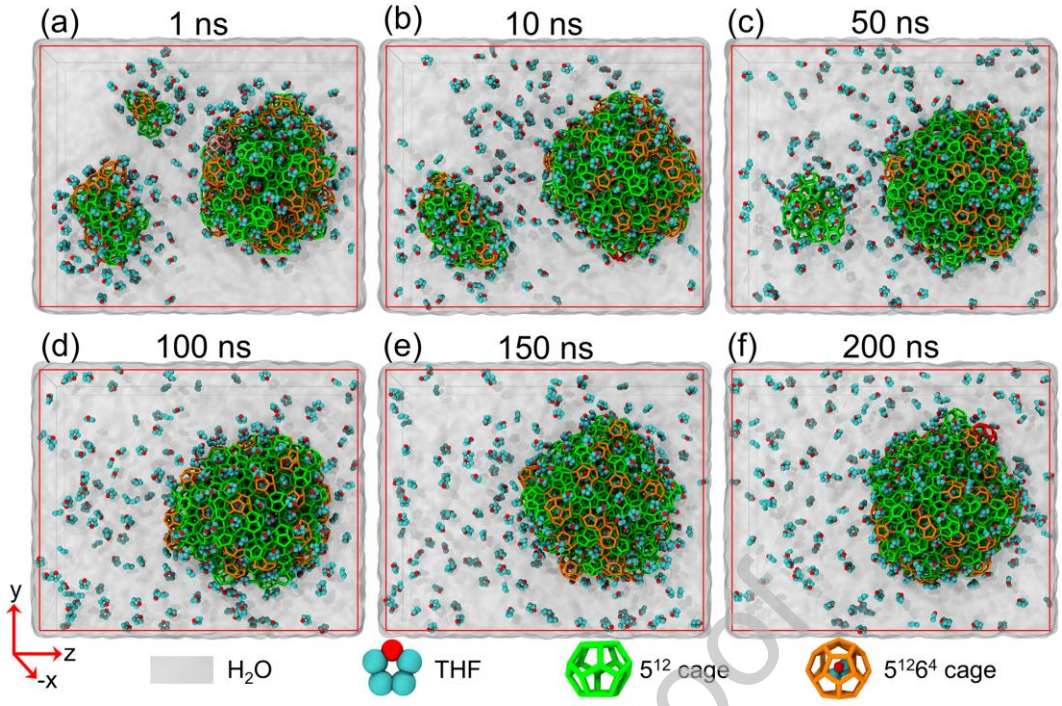

Figure 7. (a-f) Simulation snapshots showing the coarsening process of THF hydrates for the NP_{3THF} systems at different simulation times, *i.e.*, 1 ns, 10 ns, 50 ns, 100 ns, 150 ns, and 200 ns. THF is displayed as cyan (C atom) and red (O atom). Bonds of different colours represent seven types of hydrate cages, *i.e.*, green for 5^{12}, and orange for $5^{12}6^4$.

In the NP_{3THF} system, large THF hydrate nanoparticles also undergo structural reorganization and growth. Specifically, during the 0 - 1 ns of THF hydrate coarsening, the outer surface of the D_6 THF hydrate nanoparticle will quickly reorganize to a more stable state in the NP_{3THF} system. The surface area of the D_6 THF hydrate nanoparticles decreases rapidly (Figures 8(c) and S15(a-e)). But soon, with the decomposition of the D_3 and $D_{4.5}$ THF hydrate nanoparticles, the mole fraction of THF in the solution increases, thus facilitating the growth and coarsening of the D_6 THF hydrate nanoparticles (Figure S20(a-e)). It is found that the number of THF hydrate cages increases slightly during the period of 1 - 200 ns (Figures 8(d) and S16(a-e)), indicating the growth and coarsening of large THF hydrate nanoparticles. This insight can also be obtained from the F_4, volume/surface area, and number of water molecules in the cages of the D_6 THF hydrate nanoparticles in the NP_{3THF} system (Figures 8(b-c), S14(a-e), S15(a-e), S17(a-e), and S19(a-e)). In five repeated simulations for the NP_{3THF} system, the $D_{4.5}$ THF hydrate nanoparticles disappear during the period of 50 - 200 ns (Figure 8(e)). In the NP_{3THF} system, the disappearance of the $D_{4.5}$ nanoparticles occurred over a broader temporal range, yielding a mean disappearance time of 109.6 ± 35.5 ns. This higher variance, compared to the NP_{2THF} system, is attributed to the complex competitive growth environment and the stochastic nature of the collision and fusion events between the multiple dissolving and growing particles. Despite this variability, the consistent eventual disappearance of the smaller particles across all replicates provides robust evidence for the universality of the Ostwald ripening mechanism in

hydrate systems.

While the proximity of nanoparticles in the simulation box is necessitated by computational constraints, the observed trends confirm that the dissociation is a component of a larger ripening process rather than an independent artifact. The definitive evidence lies in the coupled behavior of the particles: the dissolution of smaller D_3 and $D_{4.5}$ particles coincides with a measured increase in the hydrate cage count of the D_6 nanoparticle (Figures S16-S17). This simultaneous growth and shrinkage, mediated by an increase in the THF mole fraction in the surrounding water, identifies the Gibbs-Thomson effect as the primary driving force. Furthermore, the size-dependent decomposition rates observed in the NP_{3THF} system, where smaller particles disappear more rapidly, align with the thermodynamic expectations for Ostwald ripening.

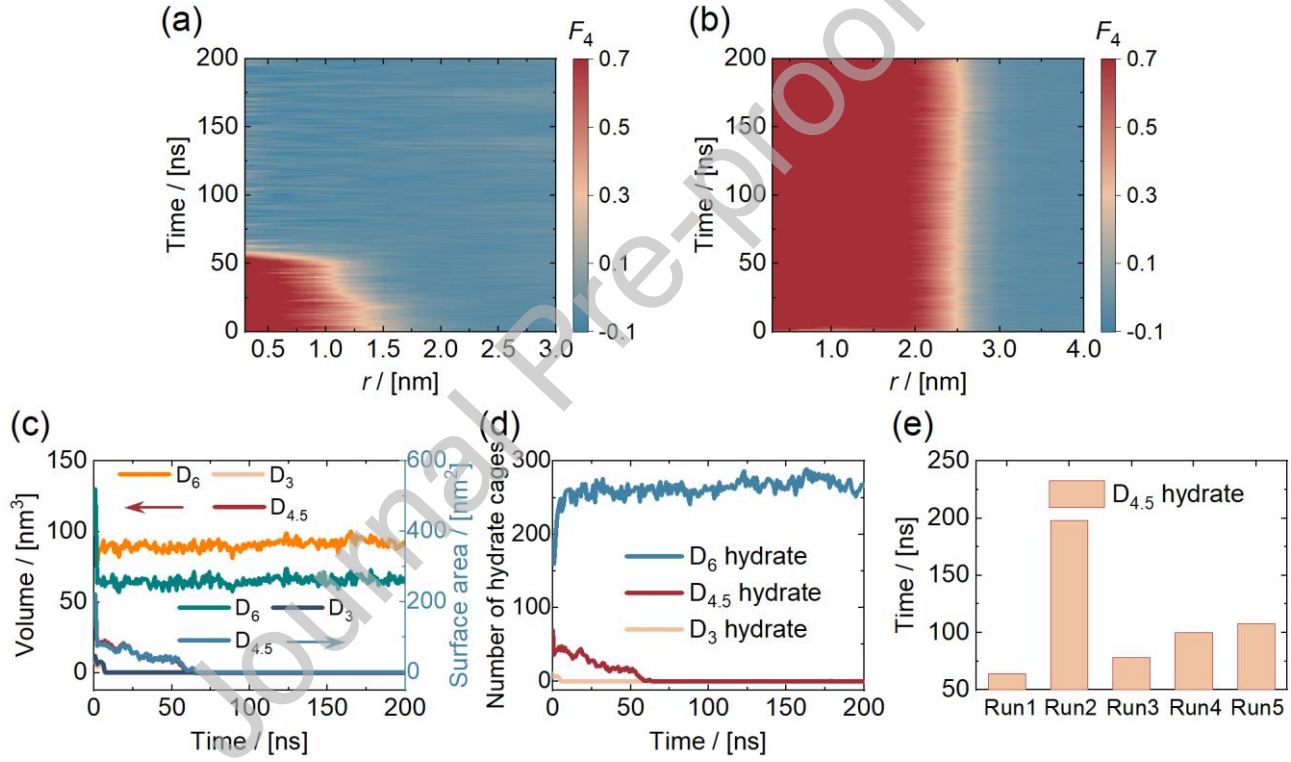

Figure 8. Time evolution of the F_4 from the center of the (a) $D_{4.5}$ and (b) D_6 THF hydrate nanoparticle for the NP_{3THF} system. Time evolution of the (c) volume/surface area of the THF hydrate nanoparticles and (d) the number of cages in the three nanoparticles for the NP_{3THF} system. (e) The time required for the complete disappearance of the $D_{4.5}$ THF hydrate nanoparticles in the five repeated simulations.

3.3 Implication for sustainable hydrate-based technologies

Sustainable hydrate-based technologies, such as H_2/CH_4 storage and transportation, CO_2 sequestration, seawater desalination, and wastewater treatment, all involve hydrate coarsening and growth. The Ostwald ripening observed during hydrate coarsening has important implications for sustainable hydrate-based technologies. The

phenomenon of small THF hydrate nanoparticles dissolving to promote the growth of large particles provides insights into the inherent limitations and potential optimization strategies for these technologies. For example, in H_2/CH_4 storage and transportation, understanding the microcosmic mechanism of hydrate particle coarsening and growth can lead to improved methods for achieving higher storage densities and more stable storage conditions. The reduction in particle count and specific surface area associated with the ripening process can alter the bulk porosity and the packing characteristics of the hydrate mass. However, larger crystals generally demonstrate superior stability and are less susceptible to spontaneous decomposition when compared to smaller nanoparticles. We can design conditions that favor the formation of large hydrate, which has the potential to increase the efficiency of gas encapsulation. To mitigate the potential challenges of uncontrolled coarsening in industrial storage systems, several active control strategies may be implemented. For instance, the introduction of chemical additives such as surfactants or anti-agglomerants can stabilize grain boundaries and restrict molecular diffusion at the interface. Furthermore, confining hydrate formation within engineered nanopores can physically limit the extent of grain coarsening, which helps to preserve a high effective surface area for rapid gas exchange. Moreover, the insights from this study can help in the development of more efficient hydrate-based CO_2 sequestration. The ability to control hydrate coarsening and growth at the nanoscale could allow for more precise engineering of hydrate structures in marine environments. This precision could result in more secure and long-term sequestration of CO_2 in hydrate form, mitigating the risks associated with leakage. In engineering practice, selecting oceanic sediments or designing artificial porous media with pore-control that prevents the formation of hydrate particles instability zone can fundamentally inhibit spontaneous lattice collapse, thereby significantly enhancing the mechanical stability of the sequestered CO_2. In the context of desalination and wastewater treatment, the knowledge gained about the stability and growth of hydrate can help optimize the selective separation processes. Enhancing the coarsening process could improve the purity of water obtained through hydrate-based desalination and wastewater treatment by reducing the entrapment of impurities within the hydrate structure. These specialized additives could be engineered to selectively destabilize the interfaces of smaller hydrate particles while lowering the surface energy of larger grains. This targeted intervention would drive the rapid migration of impurities into the liquid phase and facilitate the continuous growth of high-purity macro crystals, effectively increasing both the throughput and the water quality of desalination systems.

4. Conclusions

In this study, systematic MD simulations in bulk aqueous solution and AFM experiments at the air-water interface were performed to investigate the structural transformation of THF hydrate. The results indicate that small hydrate gradually become smaller and even disappear, whereas large hydrate remain at a large size and even grow. We provide nanoscale evidence that Ostwald ripening occurs during the growth and coarsening of clathrate hydrate, supported by simulations in the aqueous phase and topographical observations at the air-water interface. Moreover,

the decomposition of small hydrate particles goes through two stages, namely the continuous decomposition stage and the collapse decomposition stage. In the continuous decomposition stage, small THF hydrate nanoparticles decompose from the outside to the inside in sequence. When the radius of the THF hydrate nanoparticles reaches about 1 nm, the THF hydrate nanoparticles transition from the continuous decomposition stage to the collapse decomposition stage. In the collapse decomposition stage, the outside and inside of the THF hydrate nanoparticle will decompose together, *i.e.*, collapse decomposition. This nanoscale insight helps in understanding the formation mechanism of clathrate hydrate and advances the development of sustainable hydrate-based technologies (*i.e.*, H_2/CH_4 storage and transportation, CO_2 sequestration, seawater desalination, and wastewater treatment). Our study provided here can catalyze further original research, while motivating and guiding further experimental studies of sustainable hydrate-based technologies.

Declaration of competing interest

The authors declare that they have no known competing financial interests or personal relationships that could have appeared to influence the work reported in this paper.

Acknowledgements

This work was supported by the National Science Foundation for Distinguished Young Scholars (42225207), the Natural Science Foundation of Sichuan Province (2026NSFSC1161), the Research Foundation of Southwest University of Science and Technology (290-25ZX7176), and China Scholarship Council (CSC202306410133). The authors acknowledge the use of computational resources of DelftBlue supercomputer, provided by Delft High Performance Computing Centre (https://www.tudelft.nl/dhpc).

Appendix A. Supplementary data

Supplementary data to this article can be found online at https://doi.org/xxxxxxxxxxxxxxx.

References

[1] K. C. Sloan ED. Clathrate Hydrates of Natural Gases. 3rd ed. Boca Raton, FL: CRC Press, 2008.

[2] F. Mi, Z. He, G. Jiang, et al., Effect of Glucose on CH_4 Hydrate Formation in Clay Nanopores and Bulk Solution: Insights from Microsecond Molecular Dynamics Simulations, ACS Sustain Chem Eng 12 (11) (2024) 4644-4654.

[3] Y. Zhou, Y. Li, Y. Fu, et al., Nano-indentation and nano-scratch approach for precise measurements of the mechanical properties of gas hydrates, Fund Res (2026).

[4] J. Farrando-Perez, R. Balderas-Xicohtencatl, Y. Cheng, et al., Rapid and efficient hydrogen clathrate hydrate formation in confined nanospace, Nat Commun 13 (1) (2022) 5953.

[5] F. Mi, W. Li, J. Pang, et al., Molecular Insights into the Microscopic Behavior of CO_2 Hydrates in Oceanic Sediments: Implications for Carbon Sequestration, The Journal of Physical Chemistry C 128 (43) (2024) 18588-18597.

[6] Y. Zhang, H. Du, J. Zhang, et al., Progress and perspectives on pore-scale flow in methane hydrate reservoirs: Microfluidic and numerical strategies for synergistic CH_4 recovery and CO_2 sequestration, Adv Colloid Interface Sci 353 (2026) 103895.

[7] F. Mi, Z. He, F. Ning, Molecular insight on CO_2/C_3H_8 mixed hydrate formation from the brine for sustainable hydrate-based desalination, Sep Purif Technol 353 (2025) 128244.

[8] P. Babu, J. Zheng, P. Linga, et al., A Perspective on the Role of Gas Hydrates in Carbon Capture, Transport, and Sequestration, Environ Sci Technol 60 (19) (2026) 13759-13781.

[9] L. Chen, V. P. Ting, Y. Zhang, et al., Hydrate-based H2 storage with porous materials as heterogeneous promoters: state of the art and challenges, J Mater Chem A 13 (33) (2025) 27001-27049.

[10] F. Mi, Z. He, J. Pang, et al., Molecular Insights into Hybrid CH_4 Physisorption-Hydrate Formation in Spiral Halloysite Nanotubes: Implications for Energy Storage, ACS Appl Mater Interfaces 16 (49) (2024) 67587-67596.

[11] Y. Li, J. Zhang, J. Gao, et al., l-Methionine modified active ice enables ultra-rapid methane hydrate kinetics for solidified natural gas storage, Green Chem 28 (12) (2026) 5226-5239.

[12] Y. Zhang, J.-c. Feng, Y. Zhang, et al., Thermodynamics and kinetics of methane hydrate formation in seawater from the South China Sea: Potential application of hydrate-based desalination, Appl Energy 388 (2025) 125696.

[13] S. F. Li, F. Qi, K. G. Du, et al., An energy-efficient juice concentration technology by ethylene hydrate formation, Sep Purif Technol 173 (2017) 80-85.

[14] L. Sun, A. Hassanpouryouzband, H. Liang, et al., Emerging potential unconventional applications of gas hydrate technologies in sustainable and environmental industries, Renewable Sustainable Energy Rev 222 (2025) 115987.

[15] N. N. Nguyen, C. V. Nguyen, T. A. Nguyen, et al., Surface science in the research and development of hydrate-based sustainable technologies, ACS Sustain Chem Eng 10 (13) (2022) 4041-4058.

[16] A. Phan, Perspectives on Molecular Mechanisms of Hydrate Formation and Growth at Interfaces: A Mini-Review, Energy Fuels 39 (22) (2025) 10150-10164.

[17] S. Rao, Z. Li, H. Lu, et al., A review of gas hydrate formation characteristics at interfaces, Fuel 392 (2025) 134863.

[18] Y. Liu, L. Sun, C. Liu, et al., Developments and challenges in hydrate-based carbon dioxide sequestration technology, Carbon Neutrality 4 (1) (2025) 27.

[19] P. W. Voorhees, The Theory of Ostwald Ripening, J Stat Phys 38 (1-2) (1985) 231-252.

[20] M. Chaouachi, S. H. Neher, A. Falenty, et al., Time Resolved Coarsening of Clathrate Crystals: The Case of Gas Hydrates, Cryst Growth Des 17 (5) (2017) 2458-2472.

[21] M. Pan, N. A. Ismail, M. Luzi-Helbing, et al., New insights on a μm-scale into the transformation process of CH_4 hydrates to CO_2-rich mixed hydrates, Energies 13 (22) (2020) 5908.

[22] T. X. Le, M. Bornert, P. Aimedieu, et al., An experimental investigation on methane hydrate morphologies and pore

habits in sandy sediment using synchrotron X-ray computed tomography, Mar Pet Geol 122 (2020) 104646.

[23] J. S. Pandey, O. Strand, N. von Solms, et al., Direct Visualization of CH_4/CO_2 Hydrate Phase Transitions in Sandstone Pores, Cryst Growth Des 21 (5) (2021) 2793-2806.

[24] G. D. Zhang, B. J. Liu, L. Xu, et al., How porous surfaces influence the nucleation and growth of methane hydrates, Fuel 291 (2021) 120142.

[25] X. Jiang, B. J. Sun, Z. Y. Wang, et al., Methane hydrate crystal growth on shell substrate, Chin J Chem Eng 43 (2022) 50-61.

[26] L. A. Wadsworth, J. G. Balke, R. L. Hartman, et al., Carbon dioxide hydrate crystallization thickening & morphology in a micro-confined environment for carbon capture & sequestration processes, Appl Energy 371 (2024) 123664.

[27] Z. L. Xu, Y. Konno, Morphological Change of Hydrate Caused by Ostwald Ripening and Sintering, Energ Fuels 39 (9) (2025) 4238-4248.

[28] S. Dai, J. C. Santamarina, W. F. Waite, et al., Hydrate morphology: Physical properties of sands with patchy hydrate saturation, J Geophys Res-Sol Ea 117 (B11) (2012).

[29] X. Y. Chen, D. N. Espinoza, Ostwald ripening changes the pore habit and spatial variability of clathrate hydrate, Fuel 214 (2018) 614-622.

[30] X. Y. Chen, R. Verma, D. N. Espinoza, et al., Pore-Scale Determination of Gas Relative Permeability in Hydrate-Bearing Sediments Using X-Ray Computed Micro-Tomography and Lattice Boltzmann Method, Water Resour Res 54 (1) (2018) 600-608.

[31] S. Oya, M. Aifaa, R. Ohmura, Formation, growth and sintering of CO_2 hydrate crystals in liquid water with continuous CO_2 supply: Implication for subsurface CO_2 sequestration, Int J Greenhouse Gas Control 63 (2017) 386-391.

[32] L. Lei, J. C. Santamarina, Laboratory Strategies for Hydrate Formation in Fine-Grained Sediments, J Geophys Res-Sol Ea 123 (4) (2018) 2583-2596.

[33] W. Li, J. T. Pang, L. Peng, et al., Microscopic Insights into the Effects of Anti-Agglomerant Surfactants on Surface Characteristics of Tetrahydrofuran Hydrate, Energ Fuels 37 (5) (2023) 3741-3751.

[34] H. Xue, L. Li, Y. Wang, et al., Probing the critical nucleus size in tetrahydrofuran clathrate hydrate formation using surface-anchored nanoparticles, Nat Commun 15 (1) (2024) 157.

[35] Y. Guo, L. Zhou, Q. Liu, et al., Methane hydrate formation at 1 atm and 4°C on liquid-solid interfaces reveals a climate-vulnerable carbon pool, Cell Reports Physical Science 7 (1) (2026) 103030.

[36] Y. Li, Y. Zhou, Z. Zhang, et al., Stress-Induced Melting Controlled Failure Mechanisms of Methane Hydrate, Advanced Science 13 (10) (2026) e18367.

[37] X. Huang, Y. J. Deng, Z. C. Li, et al., Study of THF Hydrate Crystallization Based on In Situ Observation with Atomic Force Microscopy, Cryst Growth Des 20 (5) (2020) 2921-2929.

[38] X. Huang, Z. C. Li, Y. J. Deng, et al., Effect of Micro- and Nanobubbles on the Crystallization of THF Hydrate

Based on the Observation by Atomic Force Microscopy, J Phys Chem C 124 (25) (2020) 13966-13975.

[39] W. Li, B. Fang, Z. Tao, et al., Probing the instability of surface structure on solid Hydrates: A microscopic perspective through experiment and simulation, Appl Surf Sci 648 (2024) 158971.

[40] A. Striolo, A. Phan, M. R. Walsh, Molecular properties of interfaces relevant for clathrate hydrate agglomeration, Current Opinion in Chemical Engineering 25 (2019) 57-66.

[41] F. Mi, J. Pang, W. Li, et al., Novel pseudo-hexagonal montmorillonite model and microsecond MD simulations of hydrate formation in mixed clay sediments with surface defects, J Chem Phys 161 (21) (2024).

[42] F. Mi, H. Sun, W. Li, et al., Hybrid H2 storage in ZIF-8 and THF-driven Hydrates: A molecular simulation study at the microsecond scale, Fuel 415 (2026) 138370.

[43] T. Kraska, Direct observation of single Ostwald ripening processes by molecular dynamics simulation, J Phys Chem B 112 (39) (2008) 12408-12413.

[44] A. Hudait, V. Molinero, Ice crystallization in ultrafine water-salt aerosols: nucleation, ice-solution equilibrium, and internal structure, J Am Chem Soc 136 (22) (2014) 8081-8093.

[45] M. D. Pan, P. Naeiji, N. J. English, Fate of Nanobubbles Generated from CO_2-Hydrate Dissociation: Coexistence with Nanodroplets-A Combined Investigation from Experiment and Molecular Dynamics Simulations, Small Structures (2024) 2400080.

[46] F. Mi, Z. He, G. Jiang, et al., Effects of marine environments on methane hydrate formation in clay nanopores: A molecular dynamics study, Science of the Total Environment 852 (2022) 158454.

[47] F. Mi, F. Ning, T. J. H. Vlugt, et al., Molecular insight into hydrogen storage in clathrate hydrates: The effect of different promoters on the spontaneous nucleation of hydrogen hydrates studied via microsecond-scale molecular dynamics simulations, Chem Eng J 512 (2025) 162253.

[48] W. L. Jorgensen, D. S. Maxwell, J. TiradoRives, Development and testing of the OPLS all-atom force field on conformational energetics and properties of organic liquids, J Am Chem Soc 118 (45) (1996) 11225-11236.

[49] J. L. Abascal, E. Sanz, R. Garcia Fernandez, et al., A potential model for the study of ices and amorphous water: TIP4P/Ice, J Chem Phys 122 (23) (2005) 234511.

[50] S. Nosé, A Molecular-Dynamics Method for Simulations in the Canonical Ensemble, Mol Phys 52 (2) (1984) 255-268.

[51] M. Parrinello, A. Rahman, Crystal-Structure and Pair Potentials - a Molecular-Dynamics Study, Phys Rev Lett 45 (14) (1980) 1196-1199.

[52] M. J. Abraham, T. Murtola, R. Schulz, et al., GROMACS: High performance molecular simulations through multi-level parallelism from laptops to supercomputers, SoftwareX 1 (2015) 19-25.

[53] Y. Zhang, S. Xiao, R. Ma, et al., Characterization of the quasi-liquid layer on gas hydrates with molecular dynamics simulations, Fuel 357 (2024) 129905.

[54] X. Cai, M. Salvalaglio, A. Striolo, The quasi-liquid layer thickness controls clathrate hydrates' growth rate, Proc

Natl Acad Sci U S A 123 (11) (2026) e2521343123.

Profile of corresponding author

Dr. Fulong Ning is a Professor and Doctoral Supervisor at China University of Geosciences (Wuhan), where he serves as Dean of the School of Mechanical Engineering and Electronic Information. He is a recipient of the **National Science Fund for Distinguished Young Scholars (2022) and a Specialist under the State Council's Special Allowance Program (2023)**. Dr. Ning has been selected for several prestigious national and provincial talent programs, including the Young Top-notch Talent Support Program of the Organization Department of the CPC Central Committee, the Young Changjiang Scholar program of the Ministry of Education, and the Hubei Provincial Outstanding Contribution Award for Middle-aged and Young Experts.

Dr. Ning is currently Deputy Director of the International Joint Research Center for Deep Earth Drilling and Deep Resource Development under the Ministry of Science and Technology and Deputy Director of the Engineering Research Center for Geotechnical Drilling and Protection under the Ministry of Education. He has led over 30 national and provincial scientific research projects. As the first or corresponding author, he has published more than 100 SCI/EI-indexed papers in journals such as NC, GRL, JGR, and Science China.

BRID: 09387.00.63371

Declaration of Interest Statement

The authors declare that they have no known competing financial interests or personal relationships that could have appeared to influence the work reported in this paper.

Graphical abstract